Astron. Astrophys. 344, 472–482 (1999)

ASTRONOMY AND ASTROPHYSICS

The radio galaxies and the magnetic field in Abell 119

L. Feretti[1], D. Dallacasa[1], F. Govoni[2], G. Giovannini[1,3], G.B. Taylor[4], and U. Klein[5]

[1] Istituto di Radioastronomia del CNR, Via P. Gobetti 101, I-40129 Bologna, Italy
[2] Osservatorio Astronomico di Padova, Vicolo dell'Osservatorio 5, I-35122 Padova, Italy
[3] Dipartimento di Fisica, Universitá di Bologna, I-40100 Bologna, Italy
[4] National Radio Astronomy Observatory, P.O. Box O, Socorro, NM 87801 0387, USA
[5] Radioastronomisches Institut der Universität Bonn, Auf dem Hügel 71, D-53121 Bonn, Germany

Received 16 September 1998 / Accepted 8 January 1999

Abstract. We present new, multiwavelength Very Large Array observations of the 3 radio galaxies in the cluster Abell 119: 0053-015, 0053-016 and 3C 29. The first two radio galaxies, which lie close to the cluster center, show a narrow-angle-tailed structure, with many twists in the tails. The third radio source is located at the cluster periphery, and shows an undistorted FR I morphology. All three radio sources are strongly polarized at the highest frequencies, and all three show both more depolarization and higher Faraday Rotation Measures with increasing proximity to the cluster center. We interpret this polarization behaviour as induced by the magneto-ionized intracluster medium, whose magnetic field is estimated to be in the range 5-10 μG.

Key words: galaxies: clusters: individual: A 119 – radio continuum: galaxies – magnetic fields – galaxies: intergalactic medium

1. Introduction

The intra-cluster medium (ICM) in clusters of galaxies is known to possess magnetic fields whose origin and properties are not yet well known. The presence of cluster magnetic fields is demonstrated by a) the existence of diffuse cluster-wide radio emission (radio halo) as revealed in some clusters (e.g. Coma, see Giovannini et al. 1993, and references therein), b) the detection of Inverse Compton hard X-Ray emission (Bagchi et al. 1998, Fusco-Femiano et al. 1998), c) the study of variations of the Faraday Rotation of background sources shining through different lines of sight across the clusters, d) the analysis of Faraday Rotation gradients in extended sources embedded within the cluster.

Kim et al. (1991) analyzed the Rotation Measure (RM) of radio sources in a sample of Abell clusters and found that μG level fields are widespread in the ICM, regardless whether they do or do not have a strong radio halo. Stronger magnetic fields, from about 5 up to the extreme value of 30 μG (as in 3C 295, Perley & Taylor 1991; and Hydra A, Taylor & Perley 1993) have been found in "cooling flow" clusters where extremely large Faraday rotations have been revealed, suggesting that the generation of very strong ICM magnetic fields may be connected with the cooling flow process (Soker & Sarazin 1990, Godon et al. 1998). In the Coma cluster, a magnetic field of about $6h_{50}^{1/2}$ μG was found by Feretti et al. (1995) from the analysis of the rotation measure in the cluster radio galaxy NGC 4869. This large value is comparable to the magnetic field strength observed in cooling flow clusters, and it is considerably larger than the "equipartition" field derived by the radio data of the diffuse radio halo Coma C, permeating the Coma cluster center.

The ICM magnetic field can be tangled on scales much smaller than the typical galaxy size. Crusius-Wätzel et al. (1990), studying the depolarization in 5 strong double sources, found tangling on smaller scales (1–4 kpc). This is confirmed by the results of Feretti et al. (1995) on the Coma cluster.

The knowledge of the properties of the large-scale magnetic fields in clusters is important to study the cluster formation and evolution, and has significant implications for primordial star formation (Pudritz & Silk 1989). It has been suggested that strong fields can originate either by large scale dynamo amplification (Ruzmaikin et al. 1989) or by turbulence following a cluster merger (Tribble 1993). These magnetic fields can be traced by studying the rotation measures of radio sources located within or behind the cluster.

We examine here the cluster Abell 119, which is characterized by the presence of three extended radio galaxies, located at different projected distances from the cluster center. Two sources, 0053-015 and 0053-016, show a narrow-angle-tailed (NAT) structure of $\sim 5'$ in size, and are projected close to the cluster center. The third source, 3C 29 (0055-016), is a typical FR I, extended about 2.5′ and located at the cluster periphery. All these sources are highly polarized, therefore they are suitable for a study of the rotation measure. Moreover, their presence at different cluster locations is crucial to derive information about the magnetic field strength and structure in the whole cluster. The cluster A 119 (z=0.0441) is of richness class 1, and is classified as BM type II-III. The first ranked galaxy is UGC 579, classified as a cD galaxy (Postman & Lauer 1995, Saglia et al. 1997). According to Peres et al. (1998), no cooling flow is present in this cluster.

Send offprint requests to: lferetti@ira.bo.cnr.it

Table 1. VLA Observing Log

Name	Frequency MHz	Bandw MHz	Config.	Date	Duration Hours
A 119	1365/1515*	12.5	B	Jan96	8
	1365/1515*	12.5	C	Feb96	3
0053-015	4835/4885	50	B	Dec95-Jan96	6
	4835/4885	50	C	Feb96-Mar96	2.1
	8415/8465	50	B	Dec95-Jan96	6
	8415/8465	50	C	Feb96-Mar96	2.1
	7815/8165	50	C	Nov94	0.7
	8515/8885	50	C	Nov94	0.6
0053-016	4835/4885	50	B	Dec95-Jan96	6
	4825/4885	50	C	Feb96-Mar96	2.1
	7815/8165	50	C	Nov94	0.7
	8515/8885	50	C	Nov94	0.6
	8415/8465	50	B	Dec95-Jan96	4
	8415/8465	50	C	Feb96-Mar96	2.1
3C 29	4835/4885	50	C	Mar96	0.7
	8415/8465	50	C	Mar96	0.7

* Higher frequency IF not used because of interferences

We use a Hubble constant $H_0 = 50\,\mathrm{km\,s^{-1}\,Mpc^{-1}}$ throughout this paper. At the distance of A 119, 1 arcsec corresponds to 1.18 kpc.

2. Observations and data reduction

The data presented here were obtained with the Very Large Array (VLA) at multiple frequencies, in the B and C configurations, as given in Table 1. The source 3C 48 was used as a primary flux density calibrator. The phase calibrator was the nearby point source 0056-001, observed at intervals of about 20 minutes, while the polarization position angle calibrator was 3C 138. The instrumental polarization of the antennas was corrected using the secondary calibrator 0056-001, which was observed over a wide range of parallactic angles. A single pointing for the whole cluster at 1.365/1.515 GHz allowed us to obtain images of the two tailed radio galaxies with negligible bandwith smearing. The radio galaxy 3C 29, offset by $\sim 20'$ from the pointing position, suffers of a reduction in peak response of about 50%. The data at 1.515 GHz were seriously affected by a strong time-variable interference, which limited the sensitivity achieved in the image; therefore they were not used in the analysis. At the higher frequencies each source was observed individually. The data were reduced with the Astronomical Image Processing System (AIPS), following the standard procedure: Fourier-Transform, Clean and Restore. Self-calibration was applied to minimise the effects of amplitude and phase variations. All the images were corrected for primary beam attenuation.

Images of the Stokes parameters I, Q and U were produced at each frequency, with different resolutions, using the AIPS task IMAGR. The restoring beam was typically a circularly symmetrical Gaussian. The images of the polarized intensity $P = (Q^2 + U^2)^{1/2}$, the degree of polarization m = P/I and the position angle of polarization $\theta = 0.5 \tan^{-1}(U/Q)$ were derived from the I, Q and U images. The P maps were corrected for the positive Ricean bias due to the combination of two noisy quantities in quadrature (Wardle & Kronberg 1974). The errors deriving from off-axis primary beam polarization are always less than 1% in our sources, except in 3C 29 at 1.4 GHz. At its distance from the phase center ($\sim 20'$) the error on the polarization percentage is estimated to be within $\sim$3.5% (Napier 1989).

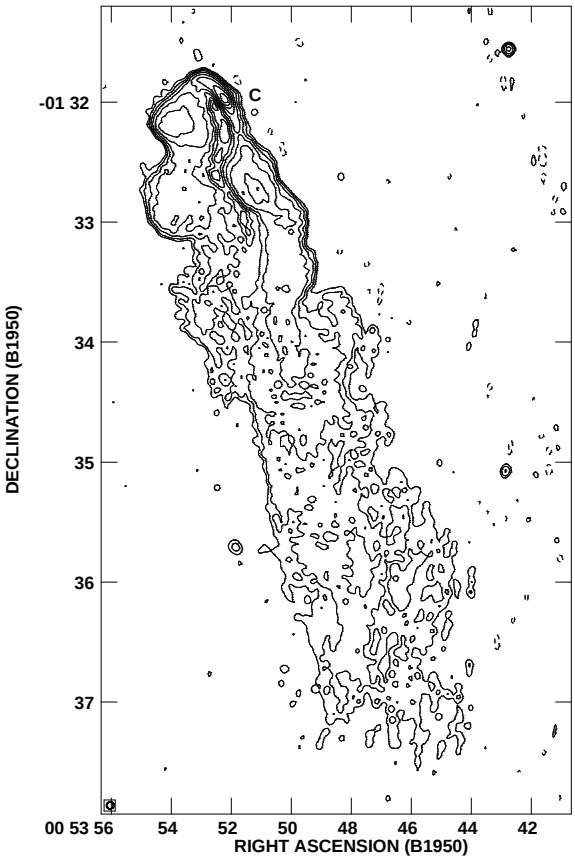

Fig. 1. Image of 0053-015 at 1.4 GHz, with angular resolution of $3.5''$. Label C indicates the core. Contour levels are -0.15, 0.15, 0.3, 0.6, 1.2, 2.5, 5, 10, 20, 40 mJy/beam. The rms noise level in this map is 38 μJy/beam.

3. Total intensity and polarization images

3.1. 0053-015

The radio galaxy 0053-015 is classified as a NAT source, with a total extent of $\sim 5'$. It was mapped at 1.4 GHz by O'Dea & Owen (1985), who found a quite irregular structure with asymmetric jets. The large scale image and the polarization information, obtained with the Effelsberg radio Telescope, were presented by Mack et al. (1993). The source is highly polarized at 10.7 GHz, the fractional polarization reaching about 30%, and a magnetic field orientation parallel to the tail direction.

The overall source structure is easily visible at 1.4 GHz, at a resolution of $3.5''$ (Fig. 1). The total extent of the source mapped at this frequency with the VLA is about $5'$, which is comparable

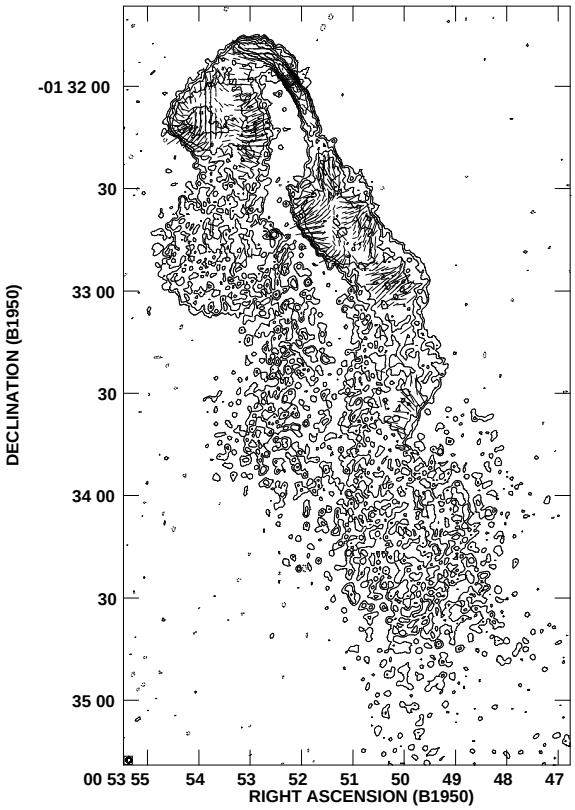

Fig. 2. Image of 0053-015 at 4.9 GHz, with angular resolution of 1.5″. Contour levels are −0.04, 0.04, 0.08, 0.15, 0.3, 0.6, 1.2, 2.5, 5, 10, 20 mJy/beam. The rms noise level is 13.5 μJy/beam. Superimposed lines represent the orientation of the polarization vector (E-field) and are proportional in length to the fractional polarization, with 1″= 10%

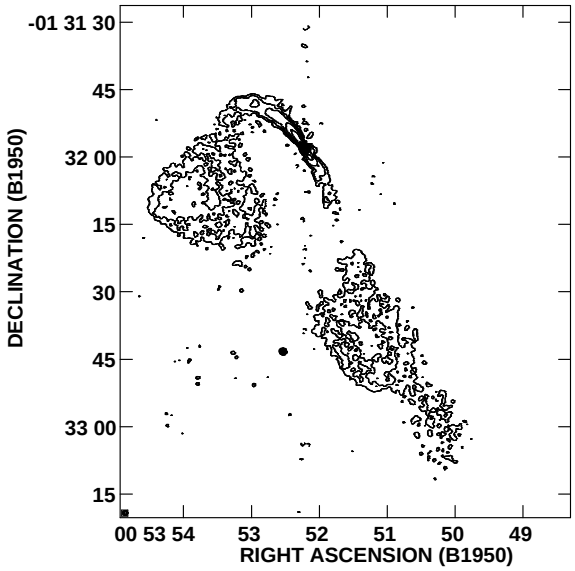

Fig. 3. Image of 0053-015 at 8.4 GHz, with angular resolution of 0.85″. Contour levels are −0.05, 0.05, 0.1, 0.2, 0.4, 0.8, 1.5, 3, 6, 12, 24 mJy/beam. The rms noise level is 10 μJy/beam.

to the extent found from the single dish image (Mack et al. 1993). The unresolved core, located in the upper western region (C in Fig. 1), is very bright in the images at all frequencies. The two short symmetric jets emanating from the core are oriented in the NE-SW direction. The NE jet bends by about 90° to the south to form a low surface brightness lobe, which expands and merges with the emission originating from the other jet. The long tail, notably rich in wiggles, smoothly fades into the noise.

The highest resolution image at 4.9 GHz, presented in Fig. 2, shows in great detail the structure of the jets and lobes. The SW jet is well collimated for about 20″, then it widens suddenly forming a well defined lobe, characterized by several bends and wiggles. The brightness of the western lobe shows a maximum at ∼50″ from the nucleus, and decreases progressively further out. The NE jet is straight at the beginning, then it sharply bends by 90°, and forms a bright large lobe. This jet is slightly brighter than the opposite one, and is easily distinguishable for about 20″. Unlike the SW jet, it is surrounded by a cocoon of lower brightness. The lobe shows a squared corner toward the east, then bends and twists, before quickly fading into the low brightness tail. Although the structure is very skewed, the properties of the two jets and lobes show some symmetries: similar length of the jets, similar distance from the nucleus of the two regions of maximum brightness in the lobes, and finally the winding structure of the tails. The jet structure is enhanced in the 8.4 GHz image (Fig. 3), where the low brightness lobes are mostly resolved out.

The source is strongly polarized at 8.4 GHz and 4.9 GHz, with similar values of the polarization percentage. In the image with 3.5″ resolution, the fractional polarization is ∼4% in the nucleus, then it oscillates between 10% and 35% along the two lobes, with values up to 50% at the lobe boundaries. At higher resolution (HPBW=1.5″), the degree of polarization is only slightly higher. At 1.4 GHz, the polarization percentage drops to values always below 10%, with irregular variations along the structure. The average depolarization, defined as the ratio between the polarization percentage at 1.4 GHz, $m_{1.4}$, and that at 4.9 GHz, $m_{4.9}$, is of ∼0.2.

3.2. 0053-016

The NAT radio galaxy 0053-016 was imaged at 1.4 GHz by O'Dea & Owen (1985), who found a total size similar to that of 0053-015 (∼5′), and a quite symmetric and regular structure. Despite the similarity of the structure of the two tails, the fractional polarization detected at 10.7 GHz by Mack et al. (1993) is very asymmetric. Significant polarized flux up to a level of 20% is found by these authors in the western source region, and in the outermost tail, while the eastern region is unpolarized. This structure in polarization has been interpreted by Mack et al. (1993) as due to depolarization within the observing beam of ∼ 1′.

In the 1.4 GHz image obtained with 3.5″ resolution (Fig. 4), the head of the source is resolved in two symmetric jets, bent backward, and without clear evidence of the nucleus (labelled as C in the figure). The jets progressively widen, and follow a helical path, before merging into a low surface brightness tail. In

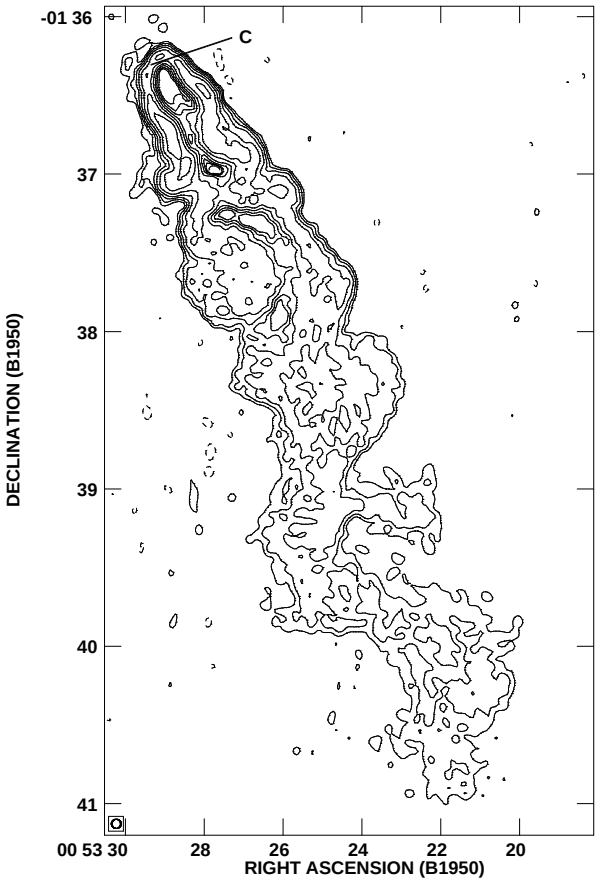

Fig. 4. Image of 0053-016 at 1.4 GHz, with angular resolution of 3.5″. Label C indicates the core. Contour levels are −0.15, 0.15, 0.3, 0.6, 1.2, 2.5, 5, 10, 20, 40 mJy/beam. The rms noise level in this map is 38 μJy/beam.

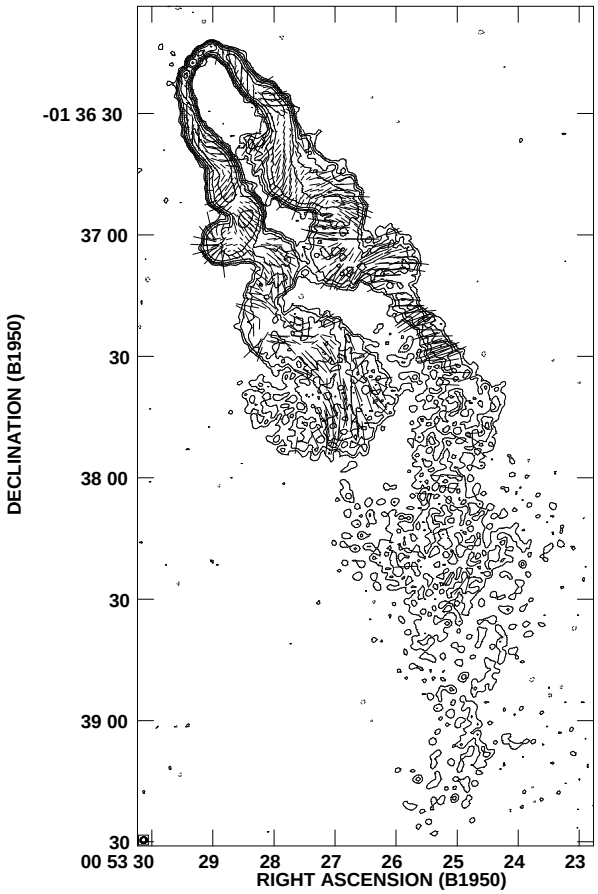

Fig. 5. Image of 0053-016 at 4.9 GHz, with angular resolution of 1.5″. Contour levels are −0.04, 0.04, 0.08, 0.15, 0.3, 0.6, 1.2, 2.5 mJy/beam. The rms noise level is 13.6 μJy/beam. Superimposed lines represent the orientation of the polarization vector (E-field) and are proportional in length to the fractional polarization, with 1″=10%

the high resolution images at higher frequencies, given in Figs. 5 and 6, the core is easily visible between the two symmetric opposite jets, initially oriented in the SE-NW direction. Both jets are curving rather continuously, but the western jet shows a slightly sharper bend at the northest point of the source, similar to 0053-015. The two jets show an increasing width, with regions of high brightness, and an extraordinarily twisted structure, up to a projected distance of about 100″ from the core. Beyond this distance, there is a remarkably straight and very collimated region in the western jet, about 20″ long (around position RA = $00^h\ 53^m\ 25.5^s$, DEC = –01° 37′ 25″), after which the jet seems to disrupt, forming a wider low surface brightness tail which is sharply bent to the south.

The core shows a polarization percentage of 6%. Both jets are higly polarized at 4.9 GHz and 8.4 GHz. At 3.5″ resolution, the fractional polarization at both frequencies oscillates between 5% and 25% for about 100″, with peaks in the bends. In the straight narrow region of the western jet, the polarization percentage increases to ∼60%. It seems clear that the high fractional polarization in this region is responsible for the polarization asymmetry detected in the Effelsberg data at 10.7 GHz (Mack et al. 1993). At the higher resolution of 1.5″ the polarization percentage is higher, thanks to the lower beam depolarization. At 1.4 GHz, the source is depolarized, with $m_{1.4}/m_{4.9}$ ∼0.5.

3.3. 3C 29 (0055-016)

This radio galaxy has been previously observed with the VLA by Morganti et al. (1993) and is classified as FR I. It is considered to be a rather isolated object (Fasano et al. 1996), in agreement with its peripheral cluster position.

The image of this galaxy at 4.9 GHz with 5″ resolution is presented in Fig. 7. It shows the central nucleus and two opposite symmetric straight jets, approximately oriented in the N-S direction. The cocoon of radio emission around the jets is typical of FR I sources (De Ruiter et al. 1990). In the image at 8.4 GHz, with the highest resolution allowed by our data (Fig. 8), the low brightness structure is still visible, and the jets are enhanced. The structure of the source magnetic field is consistent with that of FR I's. The fractional polarization at 4.9 GHz and 8.4 GHz is about 45% in the northern jet, 25% in the southern one, and reaches 50% at the lobe boundaries. At 1.4 GHz the source is still well polarized, with little depolarization ($m_{1.4}/m_{4.9} \sim 0.8$).

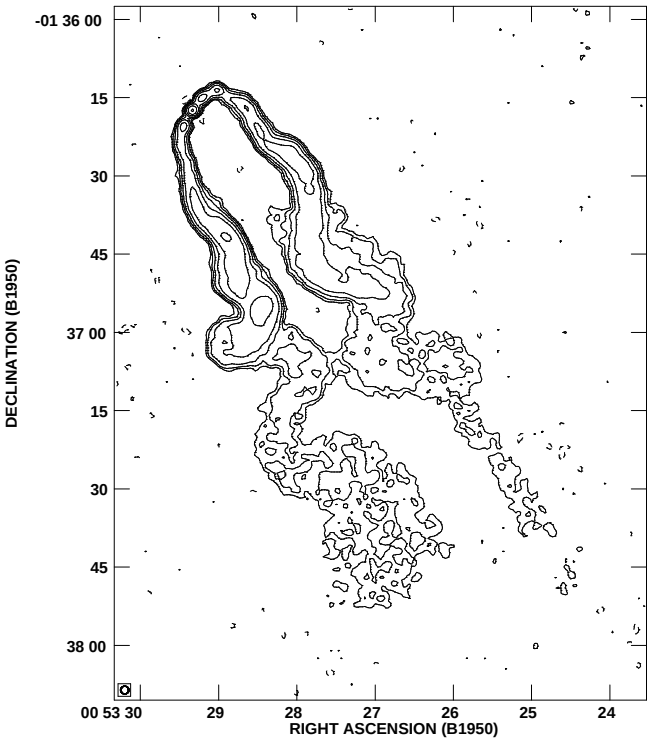

Fig. 6. Image of 0053-016 at 8.4 GHz, with angular resolution of $1.5''$. Contour levels are -0.045, 0.045, 0.09, 0.18, 0.36, 0.72, 1.5, 3 mJy/beam. The rms noise level is 14 μJy/beam.

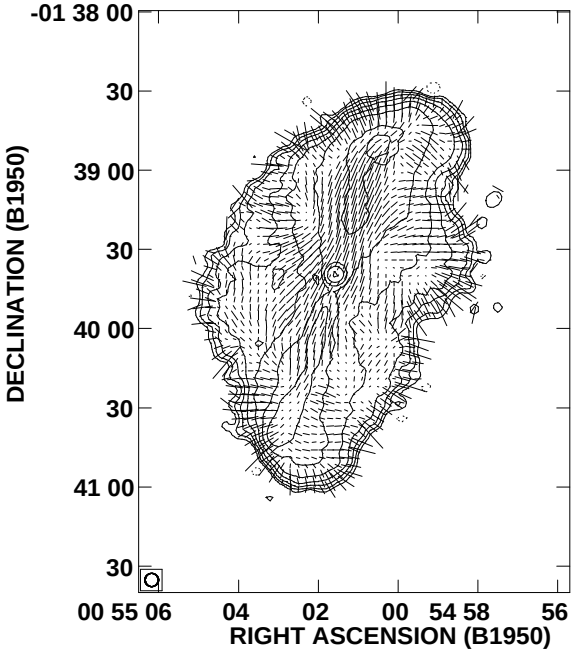

Fig. 7. Image of 3C 29 at 4.9 GHz, with angular resolution of $5''$. Contour levels are -0.25, 0.25, 0.5, 1, 2, 4, 8, 16, 32, 64 mJy/beam. The rms noise level in this map is 17 μJy/beam. The polarization vectors (E-field) are proportional in length to the fractional polarization, with $1''$ corresponding to 7%.

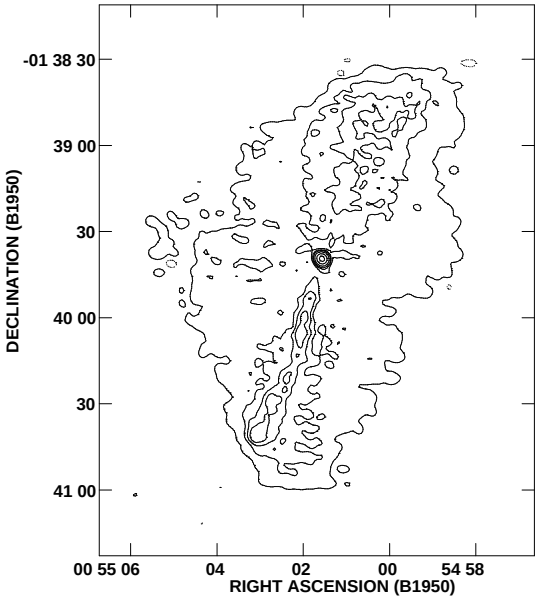

Fig. 8. Image of 3C 29 at 8.4 GHz, with angular resolution of $3''\times 2.7''(@49^\circ)$. Contour levels are -0.08, 0.08, 1.5, 3, 5, 10, 25, 50 mJy/beam. The rms noise level in this map is 13 μJy/beam.

4. Properties of the cluster radio galaxies

4.1. Spectra of the tailed radio galaxies

The point-to-point spectral index along the source structure of the two NAT's was derived using the images at 1.4 GHz, 4.9 GHz and 8.4 GHz, obtained with the angular resolution of $3.5''$ from data with matched uv-coverage. In both sources the spectrum of the core is flat with $\alpha \sim 0$. At the jet bases the spectral indices are about 0.5–0.6, and evidence of spectral curvature is found with increasing distance from the core, along the tails. The spectral indices at a distance of $\sim 2'$ are similar in the two sources, with $\alpha_{4.9}^{1.4} \sim 0.8$–0.9 and $\alpha_{8.4}^{4.9} \gtrsim 2$.

A curvature in the emission spectrum is expected as a result of synchrotron energy losses from an ensemble of electrons with an initial power-law energy distribution, and appears at a critical frequency ν_c, related to the electron age. The shape of the expected synchrotron spectrum can be computed analytically as a function of the critical frequency, the electron energy distribution index and the evolution of the electron pitch-angle distribution with time (Pacholczyk 1970). The model of Kardashev-Pacholczyk (KP) is obtained in the case that electrons maintain the same pitch angle throughout their radiative lifetime (Kardashev 1962). The model of Jaffe-Perola (JP) assumes that there is a redistribution of electron pitch angles on short time scales in comparison with their radiative lifetimes, due to their scattering on magnetic field irregularities (Jaffe & Perola 1973).

We obtained the spectra of our sources between 1.4 GHz and 8.4 GHz, at several locations along the tails up to $\sim 3'$ from the radio nucleus in 0053-015 and up to a distance of $\sim 2'$ in 0053-016. In the outermost points, only upper limits to the 8.4 GHz brightness were derived. These spectra were then fitted using both the KP and JP models, since we do not have observational evidence in favour of any of them. The fitting procedure was developed by Murgia & Fanti (1996) and applied using the same

Table 2. Optical data on radio galaxies

Name	Other	RA (B1950) h m s	DEC ° ′ ″	m_R	v_{hel} km s^{-1}	$\mid \Delta v \mid$ km s^{-1}	Proj. Dist. ′	kpc
0053-015	UGC 583	00 53 52.3	-01 31 59	12.93	11456	1697	2.4	170
0053-016	–	00 53 29.3	-01 36 17	13.89	12795	415	6.4	453
3C 29	UGC 595	00 55 01.6	-01 39 40	12.80	13491	252	21.4	1515

Caption. Columns 1 and 2: source name; Columns 3 and 4: coordinates of the galaxies from Colless at al. (1993); Column 5: red apparent magnitudes (from Saglia et al. 1997); Column 6: heliocentric velocities from Way et al. (1998); Column 7: proper velocities with respect to the average velocity of the cluster; Columns 8 and 9: projected angular and linear distance from the cluster center (given in Table 3).

Table 3. Cluster X-ray parameters

Name	RA (B1950) h m s	DEC ° ′ ″	r_c kpc	β	n_0 cm^{-3}	T keV
A 119	00 53 43.5	–01 30 59	378	0.56	1.18×10^{-3}	5.6

Caption. Columns 2 and 3: coordinates of the X-ray centroid (from Peres et al. 1998); Column 4: core radius; Column 5: ratio of the galaxy to gas temperature; Column 6: central gas density; Column 7: temperature.

approach as in Feretti et al. (1998). We used an initial electron energy distribution function of the kind $N(E)dE \propto E^{-2}dE$, corresponding to a synchrotron spectral index α=0.5

Good fits to the observed spectra were obtained by both the KP and JP model within $\sim 1'$ from the core, while at further distances the measured spectra are steeper than expected from the models. This could possibly derive from the limited sensitivity to low surface brightness structure in the 8.4 GHz image. We note also that non-uniformities in the particle and field distributions in the sources can complicate the interpretation of spectral curvature (Wiita & Gopal-Krishna 1990, Eilek & Arendt 1996).

From the values of the critical frequency and of the magnetic field, it is possible to get information on the lifetime of radiating electrons suffering synchrotron and inverse Compton losses. As the magnetic field strength, we used the equipartition value estimated at the various locations along each source. The calculation of the equipartition magnetic field involves a number of assumptions (Pacholczyk 1970). We assumed a cylindrical geometry, a volume filling factor of 1, upper and lower frequency cutoffs of 10 GHz and 10 MHz, and equal energies in the relativistic electrons and protons. In the source 0053-015, the value of the equipartition magnetic field decreases with distance from $\sim$7 μG in the inner points to $\sim$ 2.5 μG at $\sim 3'$, while the critical frequency ν_c decreases from $\gtrsim$30 GHz to $\sim$ 7 GHz. This leads to electron ages in the range 1-5 $\times$ 10^7 yr, and to an average projected bulk velocity of $\sim$ 4500 km s^{-1} in both tails. In 0053-016, the equipartition magnetic field close to the nucleus is $\sim$8.5 μG, and at $\sim 2'$ from the core is 3.8 μG in both tails. The critical frequency ranges from $\sim$ 30 GHz to $\sim$ 10 GHz, and the derived ages are about 1–4$\times10^7$ yr. This implies an average electron projected bulk velocity of $\sim$ 4000 km s^{-1}.

The relativistic electron velocities are higher than expected, as we would expect that the particles diffuse at their typical sound speed or that their motion reflects the proper motion of the parent galaxy within the cluster (see next subsection). We have also considered the possibility that the magnetic field which enters in the computation of the age is not the equipartition value. We have noted, however, that the equipartition magnetic fields in the source extremes are close to the values which give the maximum lifetimes (Van der Laan & Perola 1969), therefore the use of significantly different values of the magnetic field would make the velocity still higher.

4.2. Optical data

The host galaxies of the three radio sources studied here are all classified as ellipticals, with no particular features. The parent galaxy of 3C 29 shows round optical contours (Smith & Heckman 1989) also confirmed by the HST image (Zirbel & Baum 1998).

The dynamical analysis of the structure of A 119 has been recently presented by Way et al. (1998), who give velocities for 153 cluster galaxies and derive an average cluster velocity of 13228 km s^{-1}, and a velocity dispersion of 778 km s^{-1}. They also suggest the possible presence of subgroups. In Table 2, the positions of the optical parent galaxies are given, together with their radial heliocentric velocities. The galaxy proper velocities have been calculated with respect to the average cluster velocity. From the proper velocities of the three radio galaxies it is evident that the motion along the line of sight is quite low in 0053-016 and 3C 29. We can argue that the peripheral source 3C 29 has a genuinely low proper motion, in agreement with its undistorted structure, while the NAT 0053-016 has a predominant velocity component in the plane of the sky. In the previous subsection we found that the bulk velocity of radiating particles in the NAT galaxies is about 4000–4500 km s^{-1}. It is likely that part of this velocity reflects the proper motion of the parent galaxy within the cluster; however, it seems too high to fully account for it. The high velocities found for the electrons in the tails can be interpreted as due to: a) projection effects; b) the existence of reacceleration processes, which prevent the electron spectral index steepening and allow the electrons to extend their lifetimes; c) the presence of genuine bulk streaming motion in the radio emitting plasma; d) the existence of motion of the cluster medium (Loken et al. 1995); e) a non-uniform magnetic field, which affects the estimate of the critical frequency.

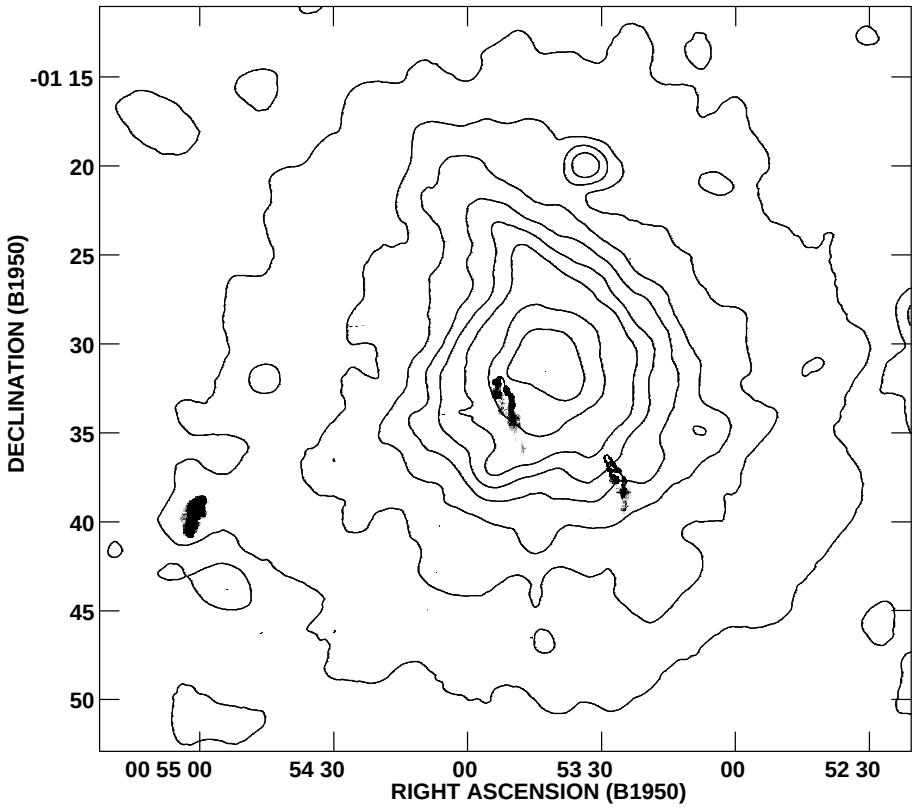

Fig. 9. The 1.4 GHz grey-scale image at 3.5″ resolution of the 3 radio galaxies discussed in this paper, overlaid upon the X-ray image from ROSAT PSPC. Contours are drawn a 8, 16, 24, 32, 40, 48, 63 and 80% of the X-ray peak.

Similar results have been found in a small sample of tailed radio galaxies by Feretti et al. (1998).

5. Comparison of X-ray and radio images

The cluster A 119 has been the target of X-ray observations with the ROSAT PSPC, for a total exposure time of 15203 sec. The data were analyzed by Cirimele et al. (1997), who fitted the X-ray brightness with a hydrostatic isothermal model of the form

$$S(r) = S_0(1 + r^2/r_c^2)^{-3\beta+0.5} \quad (1)$$

where S_0 is the central surface brightness, r_c is the core radius, and β is the ratio of the galaxy to gas temperature. They derived the parameters given in Table 3. The gas temperature in the table is from Markevitch et al. (1998), who obtained a temperature map from ASCA data, and concluded that the temperature profile of this cluster is nearly constant. We retrieved the data from the public ROSAT archive and produced an image by binning the photon event table in pixels of 15″, and by smoothing the map with a Gaussian of σ = 45″. In Fig. 9 the X-ray brightness distribution is overlaid onto the radio emission from the three cluster radio galaxies. The X-ray brightness distribution is rather irregular and asymmetric, with an extension in the northern region. The centroid of the X-ray emission (given in Table 3) is consistent with the position of the cD galaxy (Peres et al. 1998). The three radio galaxies are all embedded within the X-ray gas, at the projected distances given in Table 2. The two NAT's are located within 1.2 core radii from the cluster center, while 3C 29 is at 4 core radii, and coincides with a weak X-ray local enhancement. It is difficult to do an effective comparison between the radio emission and the X-rays, given the lower resolution of the ROSAT PSPC data. It is worth noting that the tails in both 0053-015 and 0053-016 have very similar orientations, even though the density gradient, related to the X-ray contours, is quite different. This could be related with the presence of merger-induced bulk motion of the intergalactic medium, as suggested by Bliton et al. (1998).

6. Rotation measure structure

We obtained images of the rotation measure in the radio galaxies under study by combining the suitable polarization data available to us. For the two tailed radio galaxies, 0053-015 and 0053-016, we used the maps at the 5 frequencies 4.835, 7.815, 8.165, 8.515 and 8.885 GHz, with 3.75″ resolution. In principle, the addition of the 1.365 GHz could provide a larger wavelength sampling, but the polarization of the two sources is too low at this frequency to be useful.

Following the definition $\theta_\lambda = \theta_i + RM\lambda^2$, where θ_i is the intrinsic position angle of the polarization vector and θ_λ is the position angle at wavelength λ, the value of the RM was computed by linear fitting of the polarization angle as a function of λ^2. The pixels in which the uncertainty in the polarization angle exceeds 20° were blanked. We note that only a few pixels near the source edges have such large uncertainties. The fitting algorithm provides a weighted least-squares fit, allowing for an ambiguity of $\pm n\pi$ in each polarization position angle.

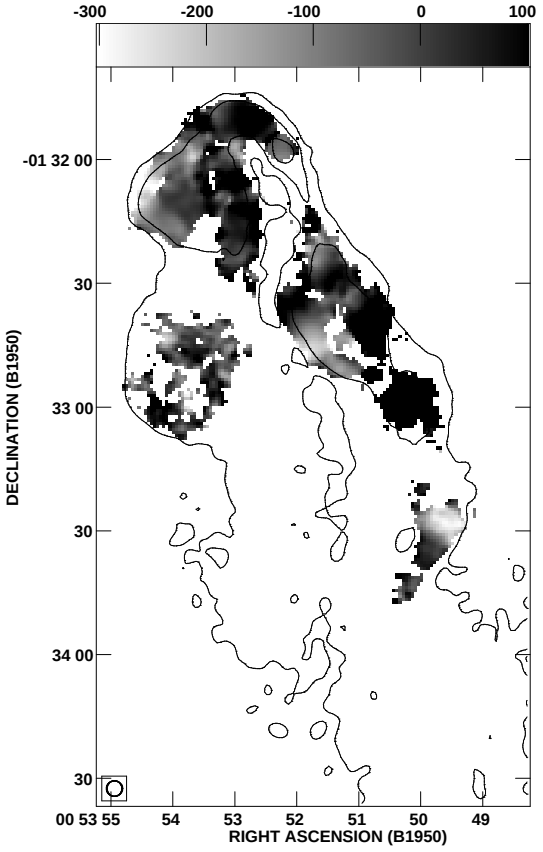

Fig. 10. Image of the rotation measure in 0053-015, computed using frequencies between 4.9 GHz and 8.9 GHz, at 3.75″ resolution. The contours refer to the total intensity image at 4.9 GHz

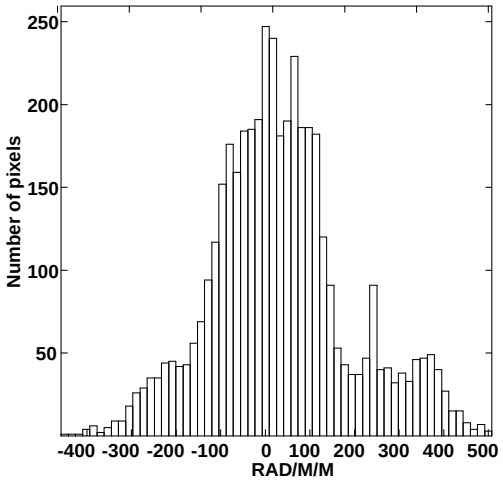

Fig. 11. Histogram of the rotation measure for all significant pixels in 0053-015

The data of both sources are well fitted by a λ^2 relation. The typical error in the resulting values of the rotation measure is ∼30 rad m^{-2}. The image of RM in 0053-015 is presented in Fig. 10. The values of RM range between –350 rad m^{-2} and +450 rad m^{-2}, and show fluctuations on small scales. The distribution of the values is evident from the histogram in Fig. 11. It is non-Gaussian, with the peak close to zero. The average RM

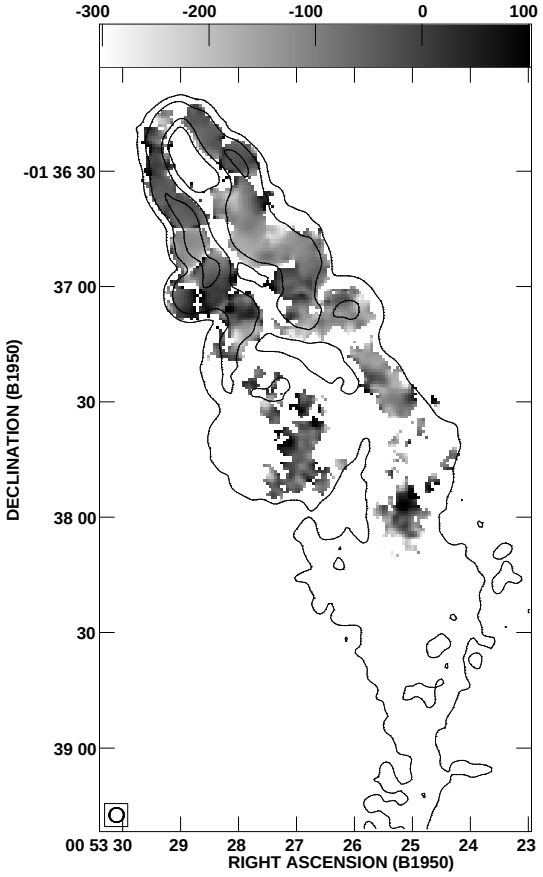

Fig. 12. Image of the rotation measure in 0053-016, computed using 5 frequencies between 4.9 GHz and 8.9 GHz, at 3.75″ resolution. The contours refer to the total intensity image at 4.9 GHz

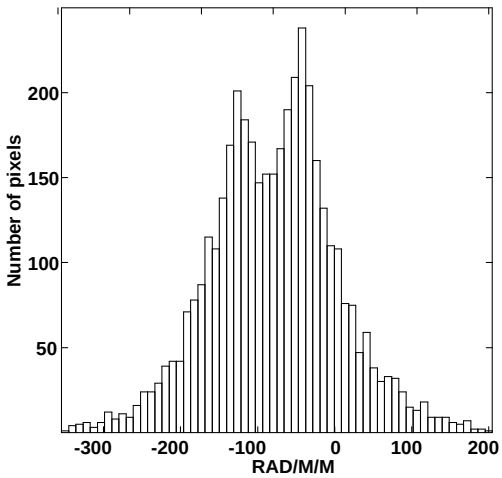

Fig. 13. Histogram of the rotation measure for all significant pixels in 0053-016

of the whole source is <RM> = + 28 rad m^{-2}, with a dispersion of σ_{RM} = 152 rad m^{-2}.

The image of RM in 0053-016 is presented in Fig. 12. The values of RM range between –300 rad m^{-2} and +200 rad m^{-2}, as displayed by the histogram of Fig. 13. The distribution of RM shows two peaks, both negative. The average RM of the whole

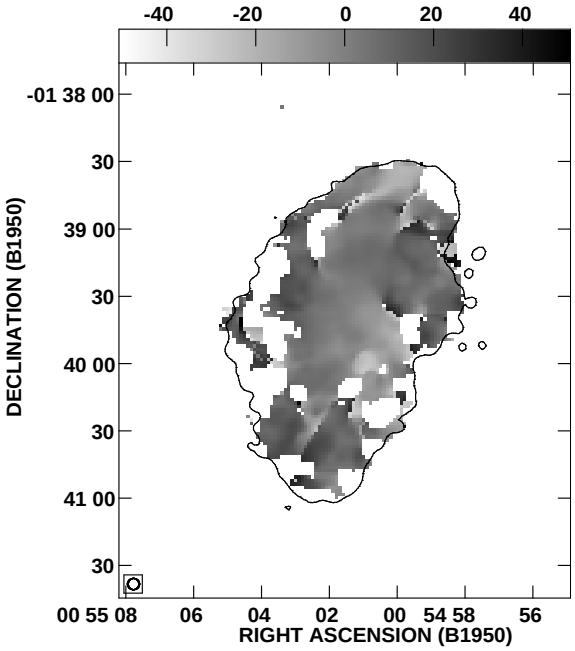

Fig. 14. Map of the rotation measure in 3c 29, computed using the 3 frequencies 1.4, 4.9 and 8.4 GHz, at 5″ resolution. The contour is the lowest total intensity contour of the image in Fig. 7

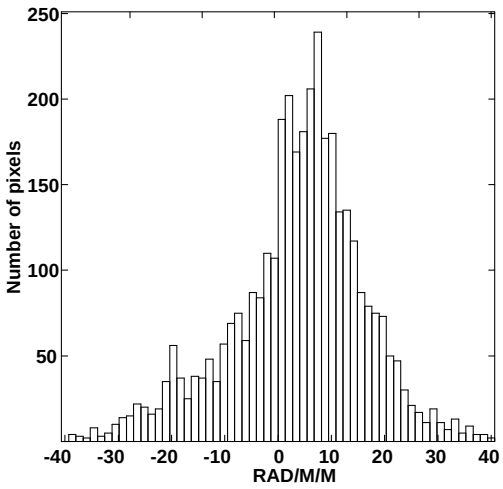

Fig. 15. Histogram of the rotation measure for all significant pixels in 3C 29

source is <RM> = –79 rad m^{-2}, with a dispersion σ_{RM} = 91 rad m^{-2}.

For 3C 29 we obtained the rotation measure by comparing the images at 1.365 GHz, 4.885 GHz and 8.440 GHz, with 5″ resolution, given that the source is highly polarized also at the low frequency. The RM in 3C 29 is rather uniform over the whole source, with values between –30 and +30 rad m^{-2} (see Figs. 14 and 15). The average value is <RM> = +4 $\pm$ 13 rad m^{-2}. The RM is therefore consistent with zero.

All the values of RM obtained in this section are likely to be genuinely related to the sources under study. The Galactic contribution to RM in the region of A 119 is in fact expected to be only $\sim$1 rad m^{-2} (Simard-Normandin et al. 1981), and therefore negligible.

Table 4. Summary of RM and depolarization data

Name	$\lvert RM_{max} \rvert$ rad m^{-2}	<RM> rad m^{-2}	σ_{RM} rad m^{-2}	DP	Dist r/r$_c$
0053-015	450	+28	152	0.2	0.45
0053-016	300	−79	91	0.5	1.20
3c 29	30	+4	13	0.8	4.01

Caption. Column 1: source name; Column 2: maximum absolute value of RM; Column 3: average value of RM; Column 4: RM dispersion; Column 5: average depolarization defined as $m_{1.4\ GHz}/m_{4.9\ GHz}$; Column 6: distance from the cluster center in units of core radii.

7. Discussion

7.1. Evidence for cluster magnetic fields

Faraday rotation in a radio source can be produced if the line of sight crosses a region of mixed magnetic field and ionized thermal gas (external Faraday rotation). In this case, the polarization angle obeys a λ^2 law over an angle larger than π/4, and the relation between the RM, the gas density n$_e$, and the magnetic field along the line of sight $B_\parallel$ is given by

$$RM = 812 \int B_\parallel n_e dl \quad \text{rad m}^{-2} \tag{2}$$

where $B_\parallel$ is measured in μG, n_e in cm^{-3} and dl in kpc. This is the case for radio sources in clusters, if the hot intracluster gas is magnetized. The RM distribution of cluster radio galaxies can therefore be used to derive information on the magnetic field along the line of sight.

In the case of a tangled magnetic field, with cells of uniform size, same strength, and random orientation, the observed RM along any given line of sight will be generated by a random walk process, and the distribution of RM results in a Gaussian with zero mean, and the dispersion related to the number of cells along the line of sight. The source will also depolarize at long wavelength, if the external Faraday screen is not fully resolved by the observing beam.

The good λ^2 fits to the polarization angle favour the interpretation that external Faraday rotation is the dominant mechanism in the present sources. In Table 4 we summarize the results for the present radio galaxies. The most striking result is the trend of RM dispersion and depolarization with distance from the cluster center. The innermost source, 0053-015, has the largest σ_{RM}, the highest absolute values of RM, and the highest depolarization at long wavelengths. The source 0053-016, located just beyond 1 core radius from the cluster center, still shows high values of RM, but lower than in 0053-015, and also the depolarization is lower. Finally, the peripheral source 3C 29 shows little RM and little depolarization. This result points to the interpretation that the external Faraday screen is the same for all 3 sources, i.e. it is the intergalactic medium in A 119, which plays

different roles according to how much magneto-ionized medium is crossed by the polarized emission. This is consistent with the two NAT's being really located in the inner cluster region, and not simply projected onto it. As suggested by Tribble (1991), unresolved external RM fluctuations produce a fall-off of the polarization degree with λ. A consistent picture is thus that the structure of the intergalactic magnetic field is tangled on small scales, this accounting for the observed depolarization. From the polarization degree of 0053-015 and 0053-016 (see Sect. 3), there is evidence that the $3.5''$ observing beam does not fully resolve the screen. Thus, we can argue that the scale of tangling of the magnetic field is <4 kpc. Moreover, field reversals must take place.

The indirect detection of the magnetic field associated with the intergalactic medium of A 119 is an important result, since so far a significant intergalactic magnetic field has been only found at the center of clusters with strong cooling flows (Ge & Owen 1993, Taylor et al. 1994). Moreover, direct evidence of a cluster magnetic field is provided in the few clusters containing a radio halo (see e.g. Feretti & Giovannini 1996). The magnetic field present in A 119 is spread on a size larger at least than one cluster core radius. The existence of a magnetic field component in the intergalactic medium therefore seems to be a common feature in clusters of galaxies.

7.2. Strength of cluster magnetic fields

The determination of the strength of the magnetic field in A 119 depends on the model for the X-ray gas distribution and on several assumptions, including the RM structure function, and the field structure.

In the simplest case that a constant magnetic field fills the whole cluster, using the central gas density and a core radius as the path-length, Eq. (2) requires $B_{\|}$ = 1.2 μG. We have found, however, that the magnetic field is likely to be tangled on scales of the order of a few kpc. In this case, the intensity of magnetic field is larger by the square root of the number of cells crossed by the line of sight.

A more realistic approach is to assume a magnetic field in randomly oriented cells of uniform size and strength, and a gas density distribution given by the hydrostatic isothermal model. The gas density n_e has the functional form

$$n_e(r) = n_0(1 + r^2/r_c^2)^{-3\beta/2} \tag{3}$$

where the parameters have the same meaning as in Eq. (1). In this case, the RM dispersion at different projected distance from the cluster center was evaluated by Felten (1996) by solving the integral of Eq. (2):

$$\sigma_{RM} = \frac{K B_{\|} n_0 r_c^{1/2} l^{1/2}}{(1 + r^2/r_c^2)^{(6\beta-1)/4}} \sqrt{\frac{\Gamma(3\beta - 0.5)}{\Gamma(3\beta)}} \tag{4}$$

where Γ is the Gamma function, r_c is the core radius in kpc, and l is the size of each cell in kpc; the central gas density n_0 is in cm^{-3} and $B_{\|}$ is in μG. The constant K depends on the integration path over the gas density distribution: K = 624, if the source lies completely beyond the cluster, and K = 441 if it is as distant from the observer as the cluster center. For the cluster A 119, using K = 441 and the gas parameters given in Table 3, the previous formula becomes

$$\sigma_{RM} \approx \frac{10.2 B_{\|} l^{1/2}}{(1 + r^2/r_c^2)^{0.59}} \tag{5}$$

The values of σ_{RM} obtained for the 2 NAT's of A 119 fit fairly well in the model described above and are consistent with a magnetic field strength in the range 9.6–13.6 μG, for a cell size between 2 and 4 kpc.

The RM of the peripheral source 3C 29 is also consistent with the previous model. However, the magnetic field probably cannot be constant over 4 core radii ($\sim$ 1.5 Mpc), otherwise the magnetic pressure would exceed the thermal pressure in the outer parts of the cluster. So it is reasonable to believe that the very low RM of 3C 29 derives not only from the low density of the foreground medium, but also from a weaker magnetic field in this region.

The model used to derive the magnetic field strength is very simplified: first, the two radio galaxies can be at different locations along the line of sight; second, the cluster shows possible substructures both in optical and in X-rays, and therefore the model used for the gas density distribution may be inaccurate; third, the magnetic field structure could be more complicated than assumed. We cannot exclude the possibility that the cell size of the magnetic field in the region around the radio galaxies would be smaller than that of the the cluster-wide magnetic field, due to the interaction between the radio sources themselves and the intergalactic medium. With cells of 10–20 kpc, the magnetic field derived from Eq. (5) is 4.5–6.1 μG.

Even allowing for the uncertainties related to the previous computations, the observational evidence favours the existence of a strong magnetic field in the intergalactic medium of A 119, over a scale larger than the cluster core radius. A plausible range for the magnetic field strength is about 5–10 μG.

8. Conclusions

Three radio galaxies belonging to the cluster Abell 119, located at different projected distance from the cluster center, are studied in total intensity and polarization. The two radio galaxies closer to the cluster center show similar NAT structure, while the most peripheral radio galaxy is a classical FR I source.

The spectra of the NAT radio galaxies progressively steepen with the distance, as expected under the effect of synchrotron energy losses. The electron lifetimes inferred from the spectral curvature lead to drift velocities of $\sim$4000–4500 km s^{-1}. Still higher values are obtained if the magnetic field is different from the equipartion value. Such large values of the velocities can derive from projection effects, or from the existence of reacceleration processes within the tails, or bulk motions along the tails and/or in the integalactic medium. We also note that non-uniformities in the magnetic field can affect the interpretation of the spectral curvature.

Large Faraday Rotations are found in the NAT's. The magnitude and scale of the RM is consistent with a magnetic field embedded in the hot X-ray emitting cluster medium. To account for the observed Faraday rotation, the cluster magnetic field must be present up to a distance of more than 1 cluster core radius. The strength of the field is between 5 and 10 μG, depending on the scale of the magnetic field tangling.

Acknowledgements. The authors thank the referee, Dr. Frazer Owen, for helpful comments. LF and GG acknowledge partial financial support from the Italian Space Agency (ASI) and from the Italian MURST. The NRAO is a facility of the National Science Foundation operated under cooperative agreement by Associated Universities, Inc.

References

Bagchi J., Pislar V., Lima Neto G.B., 1998, MNRAS 296, L23
Bliton M., Rizza E., Burns J.O., Owen F.N., Ledlow M.J., 1998, MNRAS 301, 609
Cirimele G., Nesci R., Trevese D., 1997, ApJ 475, 11
Colless M., Burstein B., Wegner G., et al., 1993, MNRAS 262, 475
Crusius-Wätzel A.R., Biermann P.L., Lerche I., Schlickeiser R., 1990, ApJ 360, 417.
De Ruiter H.R., Parma P., Fanti C., Fanti R., 1990, A&A 227, 351
Eilek J.A., Arendt P.N., 1996, ApJ 457, 105
Fasano G., Falomo R., Scarpa R., 1996, MNRAS 282, 40
Felten J.E., 1996, In: Trimble V., Reisenegger A. (eds.) Clusters, Lensing, and the Future of the Universe. ASP Conference Series, Vol. 88, p. 271
Feretti L., Giovannini G.: 1996, In: Ekers R., Fanti C., Padrielli L. (eds.) Extragalactic Radio Sources. IAU Symp. 175, Kluwer Academic Publisher, p. 333
Feretti L., Dallacasa D., Giovannini G., Tagliani A., 1995, A&A 302, 680
Feretti L., Giovannini G., Klein U., et al., 1998, A&A 331, 475
Fusco-Femiano R., Dal Fiume D., Feretti L., et al., 1998, Proceedings of 32nd COSPAR Scientific Assembly, Nagoya, Japan, in press, astro-ph/9808012
Ge J.P., Owen F.N., 1993, AJ 105, 778
Giovannini G., Feretti L., Venturi T., Kim K.-T., Kronberg P.P., 1993, ApJ 406, 399
Godon P., Soker N., White R.E. III, 1998, ApJ 116, 37
Jaffe W.J., Perola G.C., 1973, A&A 26, 423
Kardashev N.S., 1962, Sov. Astron. AJ 6, 317
Kim K.T., Tribble P.C., Kronberg P.P., 1991, ApJ 379, 80
Loken C., Roettiger K., Burns J.O., Norman M., 1995, ApJ 445, 80
Mack K.-H., Feretti L., Giovannini G., Klein U, 1993, A&A 280, 63
Markevitch M., Forman W.R., Sarazin C.L., Vikhlinin A., 1998, ApJ 503, 77
Morganti R., Killeen N.E.B., Tadhunter C.N., 1993, MNRAS 263, 1023
Murgia M., Fanti R., 1996, Internal Technical Report IRA 228/96
Napier J.P., 1989, In: Perley R.A., Schwab F.R., Bridle A.H. (eds.) Synthesis Imaging in Radio Astronomy. Astron. Soc. of the Pacific Conf. Ser., Vol. 6, p. 39
O'Dea C.P., Owen F.N., 1985, AJ 90, 927
Pacholczyk A.G., 1970, Radio Astrophysics. Freeman, San Francisco
Peres C.B., Fabian A.C., Edge A.C., Allen S.W., Johnstone R.M., 1998, MNRAS 298, 416
Perley R.A., Taylor G.B., 1991, AJ 101, 1623
Postman M., Lauer T.R., 1995, ApJ 440, 28
Pudritz R.E., Silk J., 1989, ApJ 342, 650
Ruzmaikin A., Sokoloff D., Shukurov A., 1989, MNRAS 241, 1
Saglia R.P., Burstein D., Baggley G., et al., 1997, MNRAS 292, 499
Simard-Normandin M., Kronberg P.P., Button S., 1981, ApJS 45,97
Soker N., Sarazin C.L., 1990, ApJ 348, 73
Smith E.P., Heckman T.M., 1989, ApJS 69, 365
Taylor G.B., Perley R.A., 1993, ApJ 416, 554
Taylor G.B., Barton E.J., Ge J.P., 1994, AJ 107, 1942
Tribble P.C., 1991, MNRAS 250, 726
Tribble P.C., 1993, MNRAS 263, 31
Van der Laan H., Perola G.C., 1969, A&A 3, 468
Wardle J.F.C., Kronberg P.P., 1974, ApJ 249, 255
Way M.J., Quintana H., Infante L., 1998, Submitted to AJ, astroph/9709036
Wiita P.J., Gopal-Krishna, 1990, ApJ 353, 476
Zirbel E.L., Baum S.A., 1998, ApJS 114, 177